ACS Sustainable Chemistry & Engineering

Research Article

Cite This: ACS Sustainable Chem. Eng. 2019, 7, 19295−19302

pubs.acs.org/journal/ascecg

# Unraveling the Catalytic and Plasmonic Roles of g-$C_3N_4$ Supported Ag and Au Nanoparticles Under Selective Photoexcitation

Trishamoni Kashyap, Sweety Biswasi, Arup Ratan Pal, and Biswajit Choudhury*

Physical Sciences Division, Institute of Advanced Study in Science and Technology (IASST), Paschim Boragaon, Guwahati 781035, Assam, India

Supporting Information

**ABSTRACT:** Herein, the photocatalytic roles of silver (Ag) and gold (Au) nanoparticles (NPs) on graphitic carbon nitride (CN) nanosheets are thoroughly investigated under UV (250−380 nm), UV−vis (256−600 nm), and green laser (532 nm). Under UV light, Ag and Au NPs capture photogenerated electrons from CN and function as cocatalysts. The dual roles of Ag and Au, as cocatalyst as well as a plasmonic photocatalyst, lead to reduced RhB degradation under UV−vis light. Band-gap excitation occurs in unison with surface plasmon resonance (SPR) under UV−vis light. The synchronicity leads to forward and back electron transfer at the metal−semiconductor junction, thus increasing interfacial carrier recombination. The plasmonic systems show the best result under visible light (532 nm). Plasmonic hot-electron injection from metal to CN triggers the SPR-driven photocatalysis. The photoconductivity current−voltage ($I$−$V$) measurement indicates enhanced free-carrier generation under white light (400−730 nm) as well as under selective excitations at 405, 470, and 530 nm. These freely available carriers actively participate in photocatalysis.

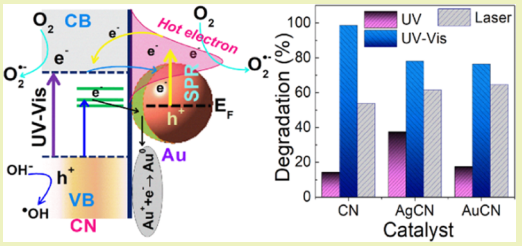


**KEYWORDS:** *photocatalytic, surface plasmon, photoluminescence, photoresponse, defects*

## INTRODUCTION

In 1972, Fujishima and Honda presented their seminal work on photoelectrochemical water splitting under UV light irradiation using a $TiO_2$ electrode.[1] Although $TiO_2$ works remarkably well under UV light, it fails measurably under visible illumination. The underlying reason is the inability of the wide band-gap (~3.2 eV) $TiO_2$ to absorb visible light. Henceforth, different strategies have been adopted to improve the visible-light absorption in $TiO_2$. Some of the methods are doping with metals and nonmetals, composites with various semiconductors, and defect engineering by vacuum calcination and hydrogenation.[2−5] Very recently, plasmonic photocatalysis has emerged as a new branch of heterogeneous photocatalysis. In plasmonic photocatalysis, the surface plasmon resonance (SPR) properties of noble metal nanoparticles (NPs) are exploited to drive photochemical reactions in the UV−vis to near-infrared (NIR) region.[6] SPR of noble metal NPs is a unique example of light−matter interactions at the nanoscale confinement.[6,7] SPR absorption can be suitably tailored from UV−vis to NIR by varying the size, shape, and alternation of the dielectric function around the metal NPs.[6] Au and Ag NPs decorated semiconductor is a promising photocatalyst for SPR activated water splitting, water purification, and $CO_2$ reduction.[8−10] Plasmonic metals show dual photocatalytic performance by a change in the excitation wavelength.[11] Under UV light excitation, the metal nanoparticles capture the photogenerated electrons from the semiconductor and thus behave as a cocatalyst. When the light wavelength switches from UV to visible, SPR of metal nanoparticles is activated. Thus, the SPR decay and semiconductor excitation decide the efficacy of the photocatalytic process under visible light.[10] The SPR-mediated photocatalysis is activated via either (1) plasmonic excitation and hot-electron injections from metal to semiconductor or (2) plasmon-induced resonance energy transfer (PIRET) from metal to semiconductor. The primary criterion for PIRET is matching of plasmon resonance energy with the band gap of the semiconductor.[12,13]

In this study, we have demonstrated the photocatalytic performance of Au and Ag NPs supported CN nanosheets. The layered CN nanosheets are evolving as a wonder photocatalyst under visible light.[14] The stacked layers provide random charge migration and accelerate carrier recombination, leading to a diminution in the photocatalytic efficiency of the system.[15] The improvement in directional charge movement and charge separation is achieved through thermal exfoliation, interlayer ion-intercalation, and cofunctionalization with doping of cations/anions.[15−17] Plasmonic decoration renders CN nanosheets an extended absorption from the visible to NIR region. Hence, we have demonstrated the photocatalytic activity of the plasmonic systems under UV, UV−vis, and a green laser. UV excitation promotes electron transfer from the conduction band (CB) of CN to Ag and Au NPs, wherein the captured electrons participate in photocatalysis. A combination of UV and visible light improves the photocatalytic activity of CN but lowers the efficiency of the plasmonic catalysts. A

Received: September 29, 2019
Published: October 29, 2019






DOI: 10.1021/acssuschemeng.9b05823
ACS Sustainable Chem. Eng. 2019, 7, 19295−19302

unison of band gap and surface plasmon activation facilitates enhanced interfacial carrier recombination in the plasmonic systems. SPR-mediated photocatalytic enhancement under visible light (532 nm) shows the active roles of plasmonic hot electrons. The free-carrier generation under band-gap and plasmonic excitation is verified by photoconductivity measurement. Strong photocurrent response is measured under white light (400−730 nm) and selective excitations at 405, 470, and 530 nm.

## EXPERIMENTAL SECTION

**Synthesis Details.** CN nanosheets were prepared at 520 °C from urea. The detailed synthesis procedure has been described in our earlier report.[18] The deposition of Ag and Au over the as-synthesized CN was conducted through an in situ method.[10] For this, 0.5 mM gold chloride solution was prepared in 100 mL of water with gold(III) chloride trihydrate ($HAuCl_4 \cdot 3H_2O$, Sigma-Aldrich) as the precursor. To the boiling solution, 30 mM trisodium citrate (Merck, India) solution was added dropwise. It was followed by the addition of 200 mg of CN while stirring. The reaction was stopped after an hour. The final product was washed and collected by centrifugation, followed by drying in an oven at 60 °C. For the synthesis of Ag NPs, we took silver nitrate precursor. The Au NPs and Ag NPs decorated CN prepared from 0.5 mM gold and silver salts were labeled as AuCN and AgCN, respectively.

**Characterization Details.** The characterization details are included in Section S1 (Supporting Information).

**Photocatalytic Details.** The photocatalytic activity of the catalysts (CN, AuCN, AgCN) was examined by monitoring the degradation of RhB dye. The details of the photocatalytic experiment under UV, UV−vis, and green laser are included in Section S2 (Supporting Information). The photocatalytic arrangement under green laser is shown in Figure S1 (Supporting Information). The details of the radical scavenging test are mentioned in Section S3.

**Photoconductivity Measurement.** Photoconductivity measurement was conducted under white light and selective excitations at 405, 470, and 530 nm. A detailed procedure is elaborated in Section S4 (Supporting Information).

## RESULTS AND DISCUSSION

We have measured the flake size and the thickness of the synthesized CN nanosheets with atomic force microscopy (AFM). The average flake size is 224 nm (Figure S2a). Surface roughness analysis of two different flakes gives average thicknesses of 8.2 and 12.3 nm (Figure S2b,c). A high-resolution transmission electron microscopy (TEM) image also shows stacking of 18 layers in corrugated nanosheets of CN (Figure S3). The diffraction patterns of CN, AgCN, and AuCN are shown in Figure S4a. The primary and minor diffraction peaks in CN at $2\theta$ = 27.7 and 13° correspond to the (002) and (100) lattice planes. These indexes give a measure of the interlayer separation and the on-plane distance between *s*-heptazine units.[18] The diffraction peaks of Au and Ag NPs are the characteristic of their crystalline cubic phases.[10] The Fourier transform infrared (FTIR) spectra of the samples are shown in Figure S4b. The individual spectrum contains two characteristic spectral ranges: 2500−4000 and 400−2000 $cm^{-1}$. The absorption bands between 2500 and 4000 $cm^{-1}$ comprise surface adsorbed −OH/$H_2O$ and secondary −NH/$NH_2$ vibrations. The bands appearing between 400 and 2500 $cm^{-1}$ are the characteristics *s*-heptazine ring vibrations. Five to six peaks are marked in the fingerprint region between 1150 and 1700 $cm^{-1}$. These bands correspond to symmetric and asymmetric stretching vibrations of C−N−C and C−NH−C bonds in the aromatic ring.[10,18−20] The sharp band at 812 $cm^{-1}$ is the breathing vibration mode of the aromatic ring.[18] There is no such change in the FTIR spectra of CN after Au and Ag NPs decoration. The morphological features of AuCN and AgCN are revealed from their TEM images, as shown in Figure 1a−d. The low-resolution TEM image of AuCN is

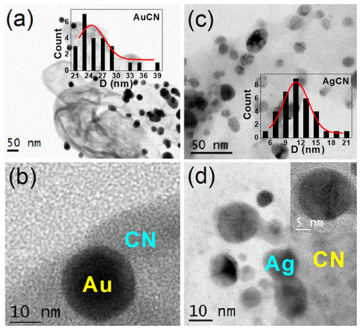


**Figure 1.** (a) Low- and (b) high-resolution TEM images of AuCN. (c) Low- and (d) high-resolution TEM images of AgCN. The inset of (d) shows the enlarged view of an Ag NP.

shown in Figure 1a. The measured average size of the Au NPs is 24 ± 0.71 nm. The high-resolution TEM image of AuCN shows a spherical Au NP over the CN nanosheets (Figure 1b). The single Au NP has a size of 23 nm. Unlike AuCN, the synthesized Ag NPs over the CN nanosheet acquire size 10.8 ± 0.17 nm (Figure 1c). The high-resolution TEM image of AgCN in Figure 1d shows the presence of nearly spherical Ag NPs over CN nanosheets. The field emission scanning electron microscope (FESEM) images of AuCN and AgCN are shown in Figure S5a,b. It clearly shows the distribution of Au and Ag NPs over the buckled CN nanosheets. We have measured the Brunauer−Emmett−Teller (BET) surface area of the photocatalysts from the $N_2$ adsorption−desorption isotherm (Figure S6). The inset of Figure S6 shows the BJH (Barrett−Joyner−Halenda) pore size distribution. The surface area and pore size of the samples are listed in Table S1. The recorded data in Table S1 shows an increase in the surface area from 64.9 in CN to 73.1 $m^2\ g^{-1}$ in AuCN and 81.8 $m^2\ g^{-1}$ in AgCN. The surface decoration of Au and Ag over CN nanosheets might have prevented nanosheet aggregation, resulting in an increased surface area. Our results are in agreement with earlier published results.[21,22]

The normalized Kubelka−Munk (FR) absorption plot of the samples in the spectral range of 200−700 nm is shown in Figure S7 (Supporting Information). A minor hump at 280 nm and a strong absorption at 370 nm complete the absorption spectra of CN. These absorptions are assigned to $\pi \rightarrow \pi^*$ and $n \rightarrow \pi^*$ electronic transitions, respectively.[18,20] Colloidal Ag and Au NPs show an active plasmon absorption band at 425 and 526 nm, respectively (inset of Figure S7).[10,23] The combination of the semiconductor absorptions and the surface plasmon band broadened the spectral window from UV−vis to NIR. The SPR bands of Ag and Au NPs show a red shift to 476 and 536 nm in AgCN and AuCN, respectively. The SPR band shift of Au and Ag NPs in a dielectric medium is described by the Maxwell−Garnet−Mie (MGM) theory.[24] The MGM theory determines the effective dielectric function of a composite medium consisting of a host matrix with NPs having different size distributions. Therefore, a change in the dielectric medium from water to CN will lead to an effective


DOI: 10.1021/acssuschemeng.9b05823
ACS Sustainable Chem. Eng. 2019, 7, 19295−19302

change in the composite dielectric function. Hence, a dielectric change will lead to spectral shift of the SPR peak.[10,23,24]

The core-level X-ray photoelectron spectra (XPS) of the samples are shown in Figure 2. Each spectrum is deconvoluted,

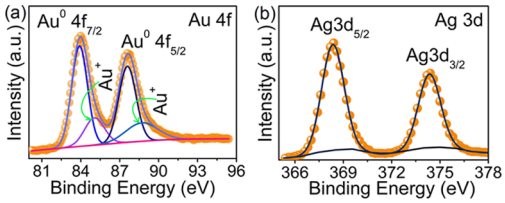


**Figure 2.** Core-level (a) Au 4f and (b) Ag 3d X-ray photoelectron spectra (XPS) of AuCN and AgCN, respectively.

and the data collected after deconvolution are shown in Table S2 (Supporting Information). Deconvolution of the C 1s peak of AgCN and AuCN gives three main peaks centering at 284.7, 288.1, and 289 eV (Figure S8a,b). The first peak corresponds to the adventitious carbon or reference carbon, the second peak to $sp^2$ C−N═C bonding in the *s*-heptazine ring, and the third peak is due to C═O bonding.[10,18,25] The N 1s spectrum in AuCN also contains three peaks at 398.7, 400.4, and 404.2 eV, which are assigned to the two-coordinated N atom ($N_{2C}$) in $sp^2$ hybridized C═N−C aromatic bonding, the three-coordinated N atom ($N_{3C}$) in the tertiary N−$(C)_3$ group, and the charged nitrogen, respectively (Figure S8c,d).[10,18] We have calculated the $N_{2C}/N_{3C}$ ratio from the peak areas of the N 1s peak. Table S2 shows the results of $N_{2C}/N_{3C}$ in pure CN from our earlier report,[18] AgCN, and AuCN. While in CN, this ratio is 0.83, in AgCN and AuCN, the values are 1.93 and 1.46, respectively. A reduction in the $N_{2C}/N_{3C}$ ratio indicates a high amount of nitrogen-vacancy defects in the $sp^2$ hybridized C═N− aromatic ring.[26] In AgCN and AuCN, these defects are compensated by the attached Au and Ag NPs. Earlier studies have shown that defects in a semiconductor provide strong metal−support interaction.[27,28] Ag and Au NPs form electrostatic binding with the nitrogen defect sites on CN. The $N_{2C}/N_{3C}$ ratio is higher in AgCN than in AuCN. It infers that Ag NPs occupy most of the nitrogenated defect sites in AgCN than those of Au NPs in AuCN. The O 1s peak at 532.1 eV (532.6 eV) in AgCN (AuCN) can be attributed to surface adsorbed water (Figure S8e, f). The deconvoluted spectrum of Au 4f contains four peaks, as shown in Figure 2a. The major doublets at 83.9 and 87.6 eV are due to Au $4f_{7/2}$ and Au $4f_{5/2}$, respectively. The separation value of 3.7 eV is in agreement with the metallic state of gold.[29] There are two other peaks at the higher binding energy sides of the metallic gold peak. These shoulder peaks can be assigned to oxidized $Au^{\delta+}$ species. According to the published reports, a binding energy difference of 1.8−2.3 eV between $Au^{\delta+}$ and $Au^{(0)}$ indicates the presence of $Au_2O_3$ ($Au^{3+}$) over metallic gold. However, this difference is between 0.7 and 1.5 eV if the oxidized species is $Au_2O$.[30−33] In Figure 2a, we have shown that this difference is only 1.1 eV, indicating that the oxidized species are possibly $Au_2O$ ($Au^+$). A recent report reveals that $Au^+$ may bind with the interfacial −OH groups and form $Au_2O$.[32] Since we have detected surface adsorbed −OH groups, these functional groups may bind with $Au^+$ and form $Au_2O$. The core-level Ag 3d spectra of AgCN show two peaks at 368.3 and 374.3 eV with a separation of 6 eV (Figure 2b). These peaks can be readily assigned to Ag $3d_{5/2}$ and Ag $3d_{3/2}$ photoemission and characterize the metallic state of silver.[29]

**Photoconductivity Measurement.** SPR decay leads to the generation of plasmonic hot electrons with energies well above the Fermi level, leaving holes in the sp band.[34−36] To understand the carrier generation by SPR decay, we conducted photoconductivity measurement for all of the samples. The photoconductivity experiment gives a measure of the plasmonic hot-electron generation from their enhanced current response. However, it does not provide a direct correlation with the improved photocatalytic activity. The reason is the differences in the experimental setup in the two tests. Photocatalysis is performed in the dye solution, whereas photoresponse is measured in solid samples with an Ohmic contact.

Figure 3 shows the results of photoconductivity of the samples under white light as well as under selective excitations

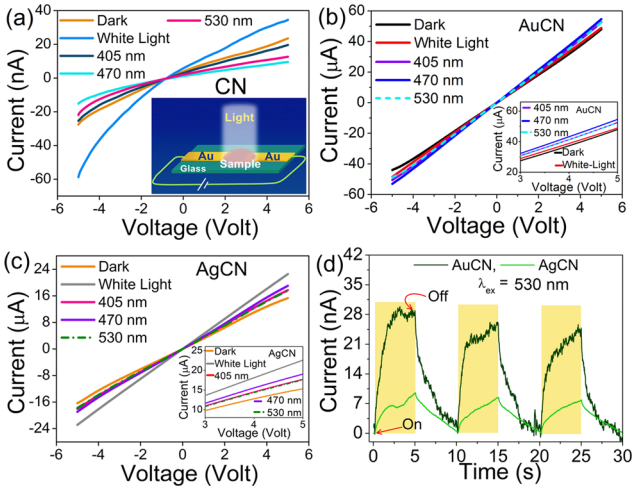


**Figure 3.** *I*−*V* curve of (a) CN, (b) AuCN, and (c) AgCN. Inset of (b) and (c) shows the expanded *I*−*V* to measure the magnitude of enhancement in photocurrent response under illumination. (d) ON−OFF study of AuCN and AgCN under 530 nm photoexcitation.

of 405, 470, and 530 nm under a bias voltage of 1 V. The schematic for the photoconductivity measurement is shown in the inset of Figure 3a. The actual photocurrent is the difference between the total current under photoexcitation minus the dark current under an applied voltage between the Au contacts. Figure 3a shows the *I*−*V* curve of CN. Photocurrent enhances under white light excitation. However, under selective excitation, there is a decrease in the current. The negative photoconductivity indicates enhanced recombination of photogenerated electrons and holes. AuCN shows a slight increase in the photocurrent under white light. However, the current response enhances under excitation of selective wavelength (Figure 3b). Similarly, AgCN also displays strong photoresponse under white light and selective photoexcitation (Figure 3c). The maximum photocurrent under white light infers the synchronous band-gap excitation in CN and SPR activation in Au and Ag NPs. We have also conducted an ON−OFF response for AuCN and AgCN under 530 nm excitation for three cycles (Figure 3d). The current response is nearly threefold stronger in AuCN than in AgCN. The stable photocurrent in AuCN is because of the SPR activation in Au under 530 nm illumination. The results of photoconductivity reveal that white light and selective photo-


DOI: 10.1021/acssuschemeng.9b05823
ACS Sustainable Chem. Eng. 2019, 7, 19295−19302

excitation generate sufficient numbers of photocarriers for participation in photocatalysis.

**Photocatalysis.** The experiments on photocatalysis have been performed under three different excitations: UV, UV−vis, and a green laser. We will discuss the results and mechanism of photocatalysis under each spectral excitation.

**UV Photocatalysis.** The changes in the absorption intensity of RhB as a function of irradiation time are shown in Figure S9. There is a monotonous decrease in the absorption intensity with irradiation time. We have measured the degradation of RhB under dark and light. The degradation of RhB under dark (Figure S10) is higher in AgCN (5.0 %) and AuCN (3.9 %) than that in CN (0.4 %). The adsorption-induced degradation of RhB in AuCN and AgCN is 9 times and 11 times stronger than that of CN. The high surface area of the composite could provide more available sites for the adsorption of RhB, leading to increased degradation. The degradation of RhB as a function of time under the UV irradiation is shown in Figure 4a. A maximum degradation of

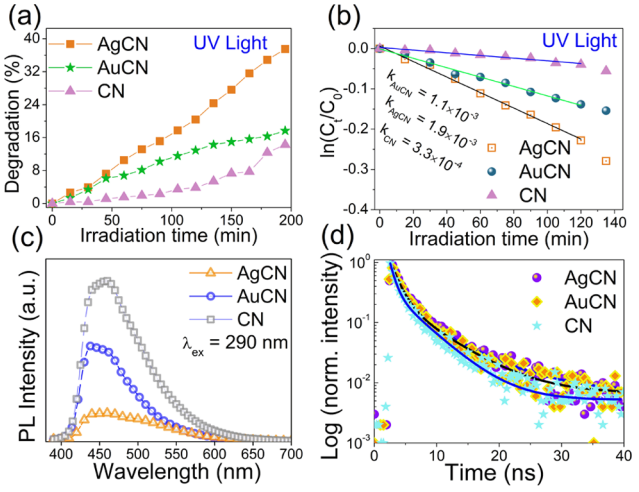


**Figure 4.** (a) Photodegradation of RhB under UV light. (b) $\ln(C_t/C_0)$ vs $t$ plot for various samples. (c) Steady-state PL spectra under a photoexcitation of 290 nm. (d) TRPL spectra of CN, AgCN, and AuCN under an excitation of 290 nm.

37.5% of RhB is recorded in the presence of AgCN. Degradation drops to 17.7 and 14.2% in AuCN and CN, respectively. Figure 4b shows the plot of $\ln(C_t/C_0)$ vs time ($t$) to measure the rate kinetics of RhB degradation. The measured rate constant for AgCN is 1.9 × 10$^{-3}$ min$^{-1}$. The value is nearly two times higher than AuCN (1.1 × 10$^{-3}$ min$^{-1}$) and more than five times higher than CN (3.3 × 10$^{-4}$ min$^{-1}$). We have proposed a schematic to describe the charge excitation and transfer under UV illumination. We have shown the process for AuCN in Figure S11. UV illumination triggers band-gap excitation and charge accumulation on CB of CN. Once photoexcited, the electrons migrate from CB to Au and Ag NPs. The metal NPs become electron-rich centers, leaving holes in the valence band (VB) of CN. The captured photoelectrons in Au and Ag are transferred to the adsorbed $O_2$ molecule. The process ends up generating superoxide radical ions ($O_2^{\bullet-}$). Experimentally, we can verify the charge separation process with the steady-state and time-resolved PL measurement. The results of the steady-state PL under UV excitation at 290 nm are shown in Figure 4c. Pristine CN shows a strong excitonic blue emission at 460 nm.[18] The peak quenches in intensity and is red-shifted by 20 nm after Au and Ag NPs decoration. The quenching in the peak intensity gives a measure of the formation of long-lived carriers after Au and Ag NPs decoration. TRPL measurement of the samples is performed at an excitation of 290 nm (Figure 4d). The results of the biexponential fitting are shown in Table S3 (Supporting Information). The average lifetime of the photoexcited carriers increases from 1.41 ns in CN to 2.47 and 3.06 ns in AuCN and AgCN, respectively. The long lifetime of carriers in AuCN and AgCN is likely due to the electron transfer from CN to Ag and Au. The electrons remain captured in the metal nanoparticles while holes remain on the valence band of CN. A recent time-resolved infrared study also reveals the production of long-lived electrons in Au−$TiO_2$ under UV excitation.[37] The comparatively short carrier lifetime in AuCN than in AgCN is because of the interfacial $Au^+$ trap states at the metallic Au−CN junction. At the interface, $Au^+$ takes up electrons from CN, leading to $Au^+ \rightarrow Au^0$ conversion on the $Au^0$ metal surface (Figure S11). Thus, fewer numbers of carriers remain on the surface of gold nanoparticles. Apart from the creation of long-lived carriers in the plasmonic hybrid, the UV excitation also triggers an interband electronic transition in Ag and Au. Because of this transition, energetic electrons rise to the upper lying states above the Fermi level. These electrons finally react with the adsorbed $O_2$ molecule and generate photoactive redox species.[38−40] The interband electronic transition is discussed in detail in UV−vis photocatalysis.

**UV−Vis Photocatalysis.** The absorption spectrum of RhB before and after UV−vis light exposure is shown in Figure S12. The arrangement and parameters for photocatalysis under UV and UV−vis are the same. The only difference is the change of the light source from UV to UV−vis. Hence, RhB degradation under dark is the same as in Figure S10. The absorption spectrum reveals a clear blue shift with irradiation time. The RhB dye undergoes photoexcitation by absorbing visible light. This self-sensitization process leads to electron injection from the excited dye species to the conduction band of CN. The electrons react with surface adsorbed $O_2$ and −OH molecules, forming reactive radical species. These reactive species attack the *N*-ethyl group of RhB, causing de-ethylation and spectral shift to the lower wavelength. The self-sensitized degradation of RhB is not prominent in the absence of a catalyst.[41] Figure 5a shows the degradation of RhB under UV−vis light. In the

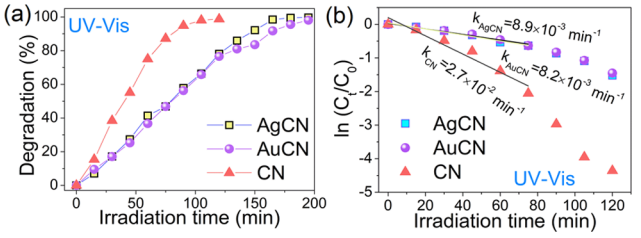


**Figure 5.** (a) Degradation curves of RhB by various catalysts under UV−vis illumination. (b) Determination of the first-order rate constant from the plot of $\ln(C_t/C_0)$ vs time.

presence of CN, RhB undergoes a rapid decrease in concentration, and nearly 98.9% degradation occurs at 120 min. The process is relatively slow in AgCN and AuCN, and it takes nearly 200 min for the complete removal of RhB. The rate of RhB degradation is 3 times faster in CN (2.7 × 10$^{-2}$



DOI: 10.1021/acssuschemeng.9b05823
ACS Sustainable Chem. Eng. 2019, 7, 19295−19302

$min^{-1}$) than that in AuCN ($8.2 \times 10^{-3}$ $min^{-1}$) and AgCN ($8.9 \times 10^{-3}$ $min^{-1}$) (Figure 5b).

Our earlier report on positron annihilation spectroscopy shows the presence of nitrogenated defect states in CN synthesized at 520 °C (Figure S13).[18] These defects are excellent trap centers of carriers. Thus, the strong catalytic activity in CN under UV−vis light (256−600 nm) is an outcome of the band-gap and sub-band-gap photoexcitation of carriers. However, photoexcitation of AgCN and AuCN under 256−600 nm triggers band-gap, sub-band-gap, as well as plasmonic excitation. Under UV−vis light (250−600 nm), the forward electron transfer from CN to the metals and plasmonic hot-electron transfer from metal to the CB of CN occur in unison (Figure 6a,b). In the 250−600 nm wavelength range,

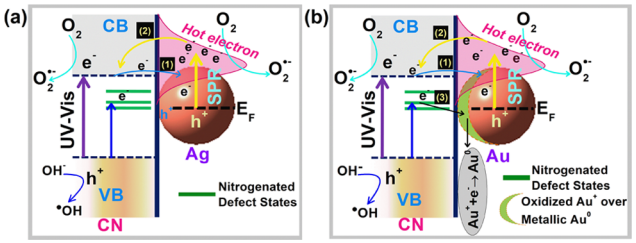


**Figure 6.** Schematic showing synchronicity of band-gap excitation and plasmonic activation under UV−vis light. The various steps involved in the photocatalysis of (a) AgCN are (1) band-gap excitation and electron transfer from CN to Ag and (2) plasmonic hot-electron generation and their subsequent transfer to CN. The photocatalytic steps involved in (b) AuCN are (1) electron transfer from CN to Au and back-transfer of hot electrons from (2) Au to CN. (3) The electrons trapped in the intermediate nitrogenated defect states in CN transfer electrons to interfacial $Au^+$ species and convert to $Au^0$.

band-gap excitation prevails below 420 nm. Photogenerated electrons in the CB of CN are transferred to Ag and Au NPs. However, in the 400−600 range, plasmonic excitation in Ag and Au is activated because of the SPR absorption of Ag (476 nm) and Au (536 nm). Surface plasmon decay leads to the generation of plasmonic hot electrons with energies well above the Fermi level, leaving holes in the sp band. These hot electrons surmount the Schottky barrier between Ag/Au and CN and flow to the conduction band of CN. At the same time, the electrons moving from CN to Ag and Au recombine with the available sp band holes. This process leads to a reduction in the number of carriers for photocatalysis. The available hot electrons on the CB participate in photocatalysis. In Figure S7, it is noticed that the SPR peak of Ag NPs overlaps the band-gap absorption in CN. The spectral overlap between SPR and the semiconductor band-gap absorption results in electric field enhancement and stimulates plasmon coupled resonance energy transfer.[42] The dipolar coupling of plasmon-exciton results in band-gap excitation in CN. The conduction band electrons again transfer to metal nanoparticles. Therefore, the forward−back transfer of electrons continues under UV−vis light, and they contribute to the overall photocatalysis.

$$M - CN \xrightarrow{UV-vis} e^-_{CB} + h^+_{VB} \text{ (band gap excitation)} \quad (1)$$

$$M - CN \xrightarrow{UV-vis} M^* - CN \text{ (plasmon activation)} \quad (2)$$

$$e^-_{CB} \xrightarrow[\text{transfer}]{\text{charge}} M^{(-)} \text{ (forward electron transfer)} \quad (3)$$

$$M^* - CN \xrightarrow[\text{transfer}]{\text{hot electron}} CN_{CB}^{(-)} \text{ (back electron transfer)} \quad (4)$$

Here M = Ag, Au. Steps 3 and 4 occur simultaneously.

Since there is no forward−backward movement of electrons in CN, we see a faster degradation and reaction kinetics in CN than that in AuCN and AgCN. However, as light exposure is extended to 195 min, sufficient numbers of hot electrons are formed near and above the Fermi levels in the plasmonic hybrids. The electrons in the CB and those available on the metal NPs interact with the $O_2$ molecule and form superoxide radicals. The holes in VB form hydroxyl radicals.[43] These superoxide and hydroxyl radicals perform RhB degradation. The reaction steps are as follows

$$M^{(-)} + O_2 \rightarrow O_2^{\bullet -} \quad (5)$$

$$CN^{(-)}_{CB} + O_2 \rightarrow O_2^{\bullet -} \quad (6)$$

$$2e^- + 2H^+ + O_2^{\bullet -} \rightarrow {}^{\bullet}OH + OH^- \quad (7)$$

$$h^+_{VB} + OH^- \rightarrow {}^{\bullet}OH \quad (8)$$

$$O_2^{\bullet -} + RhB \rightarrow \text{degradation} \quad (9)$$

$${}^{\bullet}OH + RhB \rightarrow \text{degradation} \quad (10)$$

Ag and Au NPs might also participate in the direct plasmonic photocatalysis by reacting with the adsorbed $O_2$ molecule. It so happens because of the interband electronic transition from the d to sp band under UV illumination.[38−40] The associated steps of the process are shown below.

$$Ag(\text{or } Au) + UV \xrightarrow[4d \rightarrow 5sp]{\text{interband}} Ag(\text{or } Au)^{(-)} + O_2^{\bullet -} \quad (11)$$

SPR excitation is an intraband transition of electrons in which the electrons and holes are created in the same sp band. It, thus, maximizes the recombination probability of the generated electrons and holes. In the case of interband transition, the electrons are transferred to the 5sp band, whereas holes remain in the 4d band. The hot electrons, thus formed, can directly interact with $O_2$ or cross the Schottky barrier at the metal−semiconductor interface. The process of photocatalysis is relatively slow in AuCN than in AgCN. It is because of the presence of oxidized $Au^+$ species over the surface of $Au^0$ (Figure 6b).

**Photocatalysis under Green Laser.** We have tracked the photocatalytic activity of supported plasmonic gold and silver photocatalysts under green laser at 532 nm. The absorption of RhB before and after the exposure of green laser in presence of AuCN is shown in Figure S14. The degradation of RhB under dark is 22% for CN, 25.7% for AgCN, and 33.3% for AuCN. This specific green laser irradiation does not trigger any band-gap excitation in the samples. Therefore, the overall photocatalytic results are a sum up of surface plasmon resonance (SPR) activation and sub-band-gap excitation. AuCN, being the active photocatalyst under the green laser, degrades 64.7% RhB. AgCN and CN degrade 61.5 and 53.8% of RhB (Figure 7a). AuCN shows a fast rate of photodegradation of RhB, as shown in Figure 7b. CN also shows excellent photocatalytic activity. The possible reason could be photoexcitation of electrons from VB to the nitrogenated trap states under 532 nm. The trapped carriers migrate to the surface and participate in photocatalysis. The SPR band of Ag NPs in AgCN appears at 476 nm. There is, therefore, less possibility for efficient


DOI: 10.1021/acssuschemeng.9b05823
ACS Sustainable Chem. Eng. 2019, 7, 19295−19302

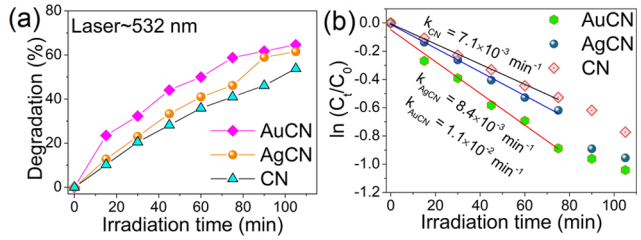


**Figure 7.** (a) Influence of green laser illumination on the photodegradation of RhB for various irradiation times. (b) $\ln(C_t/C_0)$ vs time plot to measure the first-order rate constant.

overlap of SPR of Ag with the 532 nm green laser. The plasmon activation might occur because of the presence of aggregation and varied sizes of Ag NPs. A small fraction of large NPs, which have a red-shift absorption, can match with the 532 nm photon energy. The energy absorbed is shared with the nearest Ag NPs. The enhancement of the localized field can trigger electron−hole generation in CN, which finally participates in photocatalysis. In the case of AuCN, the green laser wavelength overlaps the SPR wavelength of gold nanoparticles (536 nm). SPR activation generates energetic electrons and holes. The energetic hot electrons surpass the Schottky barrier and move to the conduction band of CN.[44] Moreover, sub-band-gap photon energy matches the SPR energy of metal nanoparticles. It will lead to a dipolar coupling between the plasmon and semiconductor, resulting in plasmonic energy transfer from metal to the semiconductor. The process generates sufficient numbers of electron−hole pairs in CN, which significantly enhances the photocatalytic activity.[45]

We have discussed the photocatalysis of AuCN and AgCN with 0.5 mM concentration of Au and Ag precursors. We have also tested the photocatalytic activity of AuCN and AgCN synthesized with 0.1 and 0.9 mM gold and silver salt concentrations. The low-resolution TEM images of $Au_{0.1}CN$, $Au_{0.9}CN$, $Ag_{0.1}CN$, and $Ag_{0.9}CN$ are shown in Figure S15. The average sizes of Ag NPs in $Ag_{0.1}CN$ and $Ag_{0.9}CN$ are 8.7 and 13.4 nm, respectively (Figure S15a,b). Similarly, the average size of Au NPs in $Au_{0.1}CN$ is 10.5 nm (Figure S15c), which is smaller than that of $Au_{0.5}CN$ (Figure 1a). Au NPs in $Au_{0.9}CN$ have a size of 30.6 nm (Figure S15d), which is larger than that of $Au_{0.5}CN$ (Figure 1a). Therefore, an increase in the concentration of the metal precursor results in particle aggregation. We also measured the absorption spectra of the samples, and the results are shown in Figure S16a,b. In AgCN, the SPR of Ag is not prominent at 0.1 mM (Figure S16a). However, the peak intensity of SPR increases if Ag NPs are prepared with an increased Ag salt concentration. We observe only a minute change in the spectral position between 0.1 and 0.5 mM in AuCN (Figure S16b). The spectral shift is prominent for Au NP prepared from 0.9 mM of the Au precursor concentration. Degradation of RhB under dark with varying concentrations of Ag and Au is shown in Figure S17a,b. Photocatalytic activity of the samples under the green laser is shown in Figure S17c,d. We have seen that 0.5 mM gives the best photocatalytic result. The weak photocatalytic activity at 0.9 mM might result from the larger size of the nanoparticles, which is led by the particle aggregation at a large salt concentration.

In our discussion, we have supposed that the photocatalysis is regulated by hydroxyl and superoxide radical species. However, to know the dominant species, we performed radical scavenging tests for AuCN (or $Au_{0.5}CN$). Di-potassium oxalate monohydrate (PO, $K_2C_2O_4{\cdot}H_2O$), *tert*-butanol ($(CH_3)_3OH$), *p*-benzoquinone (PBQ, $C_6H_4O_2$), and carbon tetrachloride ($CCl_4$) are used as hole ($h^+$), hydroxyl radical ($OH^\bullet$), superoxide radical ($O_2^-$), and electron ($e^-$) trapping agents, respectively.[20,46] The details of the radical trapping experiment have been discussed in Section S3 (Supporting Information). Figure S18 shows the degradation plot of RhB in the presence of the scavengers. In Figure 7a, we have shown that in the absence of any scavenger, AuCN degrades 64.7% RhB. The degradation reduces to 53% in the presence of *tert*-butanol, 52% in the presence of $CCl_4$, and 44.4% in the presence of PO. Surprisingly, degradation reduces to 8% when PBQ is present in solution. PBQ traps the superoxide radical and reduces the photodegradation of RhB. Thus, superoxide radicals are the dominating species in photocatalysis.

Finally, a comparison of the photocatalytic efficiency of different catalysts under UV, UV−vis, and green laser is depicted in Figure S19 (Supporting Information). In contrast to CN, the performances of AuCN and AgCN are weak under UV−vis. However, under UV and green laser, AgCN and AuCN display better performance than CN. Under UV light, Ag and Au function as cocatalysts, whereas under green laser they behave as plasmonic photocatalysts via the SPR activation.

## CONCLUSIONS

In summary, photocatalytic activities of AgCN and AuCN are investigated under UV, UV−vis, and a green laser. Illumination under UV light triggers band-gap excitation in CN. The attached metal NPs (Ag and Au) act as an electron acceptor and capture the photogenerated electrons to perform the photocatalytic reactions. Under UV−vis light, there is a synergistic promotion of band gap and surface plasmon electronic transition. The synchronous process leads to reduced photocatalytic activity in the plasmonic systems. We can see the differences in the excitonic and SPR-mediated photocatalysis under the visible (532 nm) light excitation. The strong photocatalysis in AuCN under the green laser is supported by the strong photocurrent in the ON−OFF photoresponse measurement. Under the green laser, the hot electrons injected to CN drives the photocatalytic reactions.

## ASSOCIATED CONTENT

### Supporting Information

The Supporting Information is available free of charge on the ACS Publications website at DOI: 10.1021/acssuschemeng.9b05823.

Characterization details; photocatalytic and photoconductivity details; AFM, X-ray diffraction (XRD), FTIR, TEM, FESEM, BET, UV−vis, XPS, and positron annihilation data; photocatalytic radical scavenging tests; tables for BET surface area, XPS, and time-resolved photoluminescence data (PDF)

## AUTHOR INFORMATION

### Corresponding Author

*E-mail: biswajitchoudhury@iasst.gov.in, biswa.tezu@gmail.com.

### ORCID

Biswajit Choudhury: 0000-0003-1262-6505



DOI: 10.1021/acssuschemeng.9b05823
ACS Sustainable Chem. Eng. 2019, 7, 19295−19302

## Notes

The authors declare no competing financial interest.

## ■ ACKNOWLEDGMENTS

B.C. would like to acknowledge the Department of Science & Technology (DST, Govt. of India) for providing the DST INSPIRE Faculty award. B.C. would like to acknowledge CSIR-NEIST, Jorhat, India, for providing the XPS facility.

## ■ REFERENCES

(1) Fujishima, A.; Honda, K. Electrochemical Photolysis of Water at a Semiconductor Electrode. *Nature* **1972**, *238*, 37−38.
(2) Choudhury, B.; Borah, B.; Choudhury, A. Extending Photocatalytic Activity of $TiO_2$ Nanoparticles to Visible Region of Illumination by Doping of Cerium. *Photochem. Photobiol.* **2012**, *88*, 257−264.
(3) Meng, A.; Zhu, B.; Zhong, B.; Zhang, L.; Cheng, B. Direct Z-scheme $TiO_2$/CdS Hierarchical Photocatalyst for Enhanced Photocatalytic $H_2$-Production Activity. *Appl. Surf. Sci.* **2017**, *422*, 518−527.
(4) Choudhury, B.; Bayan, S.; Choudhury, A.; Chakraborty, P. Narrowing of Band Gap and Effective Charge Carrier Separation in Oxygen Deficient $TiO_2$ Nanotubes with Improved Visible Light Photocatalytic Activity. *J. Colloid Interface Sci.* **2016**, *465*, 1−10.
(5) Zhu, G.; Shan, Y.; Lin, T.; Zhao, W.; Xu, J.; Tian, Z.; Zhang, H.; Zheng, C.; Huang, F. Hydrogenated Blue Titania with High Solar Absorption and Greatly Improved Photocatalysis. *Nanoscale* **2016**, *8*, 4705−4712.
(6) Zhang, X.; Chen, Y. L.; Liu, R.-S.; Tsai, D. P. Plasmonic Photocatalysis. *Rep. Prog. Phys.* **2013**, *76*, No. 046401.
(7) Jiang, N.; Zhuo, X.; Wang, J. Active Plasmonics: Principles, Structures, and Applications. *Chem. Rev.* **2018**, *118*, 3054−3099.
(8) Méndez-Medrano, M. G.; Kowalska, E.; Lehoux, A.; Herissan, A.; Ohtani, B.; Rau, S.; Colbeau-Justin, C.; Rodríguez-López, J. L.; Remita, H. Surface Modification of $TiO_2$ with Au Nanoclusters for Efficient Water Treatment and Hydrogen Generation under Visible Light. *J. Phys. Chem. C* **2016**, *120*, 25010−25022.
(9) Wang, T.; Lv, R.; Zhang, P.; Li, C.; Gong, J. Au Nanoparticle Sensitized ZnO Nanopencil Arrays for Photoelectrochemical Water Splitting. *Nanoscale* **2015**, *7*, 77−81.
(10) Rajender, G.; Choudhury, B.; Giri, P. K. In Situ Decoration of Plasmonic Au Nanoparticles on Graphene Quantum Dots-Graphitic Carbon Nitride Hybrid and Evaluation of Its Visible Light Photocatalytic Performance. *Nanotechnology* **2017**, *28*, No. 395703.
(11) Li, J.; Cushing, S. K.; Zheng, P.; Senty, T.; Meng, F.; Bristow, A. D.; Manivannan, A.; Wu, N. Solar Hydrogen Generation by a CdS-Au-$TiO_2$ Sandwich Nanorod Array Enhanced with Au Nanoparticle as Electron Relay and Plasmonic Photosensitizer. *J. Am. Chem. Soc.* **2014**, *136*, 8438−8449.
(12) Biroju, R. K.; Choudhury, B.; Giri, P. K. Plasmon-Enhanced Strong Visible Light Photocatalysis by Defect Engineered CVD Graphene and Graphene Oxide Physically Functionalized with Au Nanoparticles. *Catal. Sci. Technol.* **2016**, *6*, 7101−7112.
(13) Ghobadi, T. G. U.; Ghobadi, A.; Ozbay, E.; Karadas, F. Strategies for Plasmonic Hot-Electron-Driven Photoelectrochemical Water Splitting. *ChemPhotoChem* **2018**, *2*, 161−182.
(14) Choudhury, B. *Nanophotocatalysis and Environmental Applications: Materials and Technology*; Inamuddin, S. G., Kumar, A., Lichtfouse, E., Asiri, A. M., Eds.; Springer International Publishing: Cham, 2019; pp 167−209.
(15) Chen, P.; Wang, H.; Liu, H.; Ni, Z.; Li, J.; Zhou, Y.; Dong, F. Directional electron delivery and enhanced reactants activation enable efficient photocatalytic air purification on amorphous carbon nitride co-functionalized with O/La. *Appl. Catal., B* **2019**, *242*, 19−30.
(16) Li, Y.; Sun, Y.; Ho, W.; Zhang, Y.; Huang, H.; Cai, Q.; Dong, F. Highly enhanced visible-light photocatalytic $NO_x$ purification and conversion pathway on self-structurally modified g-$C_3N_4$ nanosheets. *Sci. Bull.* **2018**, *63*, 609−620.
(17) Xiong, T.; Cen, W.; Zhang, Y.; Dong, F. Bridging the g-$C_3N_4$ Interlayers for Enhanced Photocatalysis. *ACS Catal.* **2016**, *6*, 2462−2472.
(18) Choudhury, B.; Paul, K. K.; Sanyal, D.; Hazarika, A.; Giri, P. K. Evolution of Nitrogen-Related Defects in Graphitic Carbon Nitride Nanosheets Probed by Positron Annihilation and Photoluminescence Spectroscopy. *J. Phys. Chem. C* **2018**, *122*, 9209−9219.
(19) Li, H.; Jing, Y.; Ma, X.; Liu, T.; Yang, L.; Liu, B.; Yin, S.; Wei, Y.; Wang, Y. Construction of a Well-Dispersed Ag/Graphene-Like g-$C_3N_4$ Photocatalyst and Enhanced Visible Light Photocatalytic Activity. *RSC Adv.* **2017**, *7*, 8688−8693.
(20) Choudhury, B.; Giri, P. K. Isotype Heterostructure of Bulk and Nanosheets of Graphitic Carbon Nitride for Efficient Visible Light Photodegradation of Methylene Blue. *RSC Adv.* **2016**, *6*, 24976−24984.
(21) Xie, L.; Ai, Z.; Zhang, M.; Sun, R.; Zhao, W. Enhanced Hydrogen Evolution in the Presence of Plasmonic Au-Photo-Sensitized g-$C_3N_4$ with an Extended Absorption Spectrum from 460 to 640 nm. *PLoS One* **2016**, *11*, No. e0161397.
(22) Guo, Y.; Jia, H.; Yang, J.; Yin, H.; Yang, Z.; Wang, J.; Yang, B. Understanding the roles of plasmonic Au nanocrystal size, shape, aspect ratio and loading amount in Au/g-$C_3N_4$ hybrid nanostructures for photocatalytic hydrogen generation. *Phys. Chem. Chem. Phys.* **2018**, *20*, 22296−22307.
(23) Evanoff, D. D., Jr.; Chumanov, G. Synthesis and Optical Properties of Silver Nanoparticles and Arrays. *ChemPhysChem* **2005**, *6*, 1221−1231.
(24) Battie, Y.; Resano-Garcia, A.; Chaoui, N.; Zhang, Y.; En Naciri, A. Extended Maxwell-Garnett-Mie formulation applied to size dispersion of metallic nanoparticles embedded in host liquid matrix. *J. Chem. Phys.* **2014**, *140*, No. 044705.
(25) Fageria, P.; Uppala, S.; Nazir, R.; Gangopadhyay, S.; Chang, C.-H.; Basu, M.; Pande, S. Synthesis of Monometallic (Au and Pd) and Bimetallic (AuPd) Nanoparticles Using Carbon Nitride (C3N4) Quantum Dots via the Photochemical Route for Nitrophenol Reduction. *Langmuir* **2016**, *32*, 10054−10064.
(26) Niu, P.; Yin, L.-C.; Yang, Y.-Q.; Liu, G.; Cheng, H.-M. Increasing the Visible Light Absorption of Graphitic Carbon Nitride (Melon) Photocatalysts by Homogeneous Self-Modification with Nitrogen Vacancies. *Adv. Mater.* **2014**, *26*, 8046−8052.
(27) Tauster, S. J. Strong Metal-Support Interactions. *Acc. Chem. Res.* **1987**, *20*, 389−394.
(28) Tang, H.; Su, Y.; Zhang, B.; Lee, A. F.; Isaacs, M. A.; Wilson, K.; Li, L.; Ren, Y.; Huang, J.; Haruta, M.; Qiao, B.; Liu, X.; Jin, C.; Su, D.; Wang, J.; Zhang, T. Classical Strong Metal−Support Interactions Between Gold Nanoparticles and Titanium Dioxide. *Sci. Adv.* **2017**, *3*, No. e1700231.
(29) Moulder, J. F.; Chastain, J. *Handbook of X-ray Photoelectron Spectroscopy: A Reference Book of Standard Spectra for Identification and Interpretation of XPS Data*; Physical Electronics Division: Perkin-Elmer Corporation, 1992.
(30) Xiong, Z.; Zhang, L. L.; Ma, J.; Zhao, X. S. Photocatalytic Degradation of Dyes over Graphene−Gold Nanocomposites under Visible Light Irradiation. *Chem. Commun.* **2010**, *46*, 6099−6101.
(31) Tchaplyguine, M.; Mikkelä, M.-H.; Zhang, C.; Andersson, T.; Björneholm, O. Gold Oxide Nanoparticles with Variable Gold Oxidation State. *J. Phys. Chem. C* **2015**, *119*, 8937−8943.
(32) Matolín, V.; Cabala, M.; Matolínová, I.; Škoda, M.; Libra, J.; Václav, M.; Prince, K. C.; Skála, T.; Yoshikawa, H.; Yamashita, Y.; Ueda, S.; Kobayashi, K. $Au^+$and $Au^{3+}$ Ions in $CeO_2$ RF-Sputtered Thin Films. *J. Phys. D: Appl. Phys.* **2009**, *42*, No. 115301.
(33) Han, S. W.; Kim, Y.; Kim, K. Dodecanethiol-Derivatized Au/Ag Bimetallic Nanoparticles: TEM, UV/VIS, XPS, and FTIR Analysis. *J. Colloid Interface Sci.* **1998**, *208*, 272−278.
(34) Cushing, S. K.; Chen, C.-J.; Dong, C. L.; Kong, X.-T.; Govorov, A. O.; Liu, R.-S.; Wu, N. Tunable Nonthermal Distribution of Hot Electrons in a Semiconductor Injected from a Plasmonic Gold Nanostructure. *ACS Nano* **2018**, *12*, 7117−7126.


DOI: 10.1021/acssuschemeng.9b05823
*ACS Sustainable Chem. Eng.* 2019, 7, 19295−19302

(35) Paul, K. K.; Giri, P. K.; Sugimoto, H.; Fujii, M.; Choudhury, B. Evidence for Plasmonic Hot Electron Injection Induced Superior Visible Light Photocatalysis by g-$C_3N_4$ Nanosheets Decorated with Ag−$TiO_2$(B) and Au−$TiO_2$(B) Nanorods. *Sol. Energy Mater. Sol. Cells* **2019**, *201*, No. 110053.
(36) Marchuk, K.; Willets, K. A. Localized Surface Plasmons and Hot Electrons. *Chem. Phys.* **2014**, *445*, 95−104.
(37) Dai, X.; Jiao, Z.; Ma, Z.; Liu, K.; Wang, C.; Su, H. Capturing the Long-Lived Photogenerated Electrons in Au/$TiO_2$ upon UV or Visible Irradiation by Time-Resolved Infrared Spectroscopy. *J. Phys. Chem. C* **2019**, *123*, 20325−20332.
(38) Chen, X.; Zheng, Z.; Ke, X.; Jaatinen, E.; Xie, T.; Wang, D.; Guo, C.; Zhao, J.; Zhu, H. Supported Silver Nanoparticles as Photocatalysts under Ultraviolet and Visible Light Irradiation. *Green Chem.* **2010**, *12*, 414−419.
(39) Balamurugan, B.; Maruyama, T. Evidence of an Enhanced Interband Absorption in Au Nanoparticles: Size-dependent Electronic Structure and Optical properties. *Appl. Phys. Lett.* **2005**, *87*, No. 143105.
(40) Hou, W.; Hung, W. H.; Pavaskar, P.; Goeppert, A.; Aykol, M.; Cronin, S. B. Photocatalytic Conversion of $CO_2$ to Hydrocarbon Fuels via Plasmon-Enhanced Absorption and Metallic Interband Transitions. *ACS Catal.* **2011**, *1*, 929−936.
(41) Wu, T.; Liu, G.; Zhao, J.; Hidaka, H.; Serpone, N. Photoassisted Degradation of Dye Pollutants. V. Self-Photosensitized Oxidative Transformation of Rhodamine B under Visible Light Irradiation in Aqueous $TiO_2$ Dispersions. *J. Phys. Chem. B* **1998**, *102*, 5845−5851.
(42) Wang, M.; Ye, M.; Iocozzia, J.; Lin, C.; Lin, Z. Plasmon-Mediated Solar Energy Conversion via Photocatalysis in Noble Metal/Semiconductor Composites. *Adv. Sci.* **2016**, *3*, No. 1600024.
(43) Ma, H.; Feng, J.; Jin, F.; Wei, M.; Liu, C.; Ma, Y. Where Do Photogenerated Holes at the g-$C_3N_4$/Water Interface Go for Water Splitting: $H_2O$ or $OH^-$? *Nanoscale* **2018**, *10*, 15624−15631.
(44) Besteiro, L. V.; Govorov, A. O. Amplified Generation of Hot Electrons and Quantum Surface Effects in Nanoparticle Dimers with Plasmonic Hot Spots. *J. Phys. Chem. C* **2016**, *120*, 19329−19339.
(45) Cushing, S. K.; Li, J.; Meng, F.; Senty, T. R.; Suri, S.; Zhi, M.; Li, M.; Bristow, A. D.; Wu, N. Photocatalytic Activity Enhanced by Plasmonic Resonant Energy Transfer from Metal to Semiconductor. *J. Am. Chem. Soc.* **2012**, *134*, 15033−15041.
(46) Schneider, J.; Bahnemann, D. W. Undesired Role of Sacrificial Reagents in Photocatalysis. *J. Phys. Chem. Lett.* **2013**, *4*, 3479−3483.


DOI: 10.1021/acssuschemeng.9b05823
*ACS Sustainable Chem. Eng.* 2019, 7, 19295−19302